

*Full Length Research Paper*

# **Optical and scanning kelvin probe microscopic characterization of sol-gel synthesized aluminum doped zinc cobalt ferrite nanoparticles**

**Butembu Sabastine<sup>1</sup>, Osamong Gideon Akou<sup>1</sup>, Kamweru Paul Kuria<sup>1\*</sup>, Gichumbi Joel Mwangi<sup>1</sup> and Ndiritu Francis<sup>1,2</sup>**

<sup>1</sup>Department of Physical Sciences, Chuka University, Nairobi - Meru, Chuka, Kenya.

<sup>2</sup>Department of Physics, Egerton University, Biashara kilimo, Kenya.

Received 29 May, 2020; Accepted 30 July, 2020

**In this work,  $Zn_{1-x}CoFe_2Al_xO_4$  ( $x=0, 0.2, 0.4, 0.6, 0.8$  and  $1.0$ ) ferrites were synthesized using the sol-gel method. XRD analysis was done and confirmed the formation of spinel structure, where the particle size and lattice parameter decrease with increase of aluminum concentration. This may be attributed to a shift of the bigger  $Al^{3+}$  ions, from the tetrahedral to the octahedral sites, interchanging with smaller  $Zn^{2+}$  ions and that consequently result to a decreased unit cell size. The Scanning Kelvin Probe Microscopy (SKPM) showed that the work function average ranges between 200 and 680 mV for the different concentration of aluminum in the samples. Fractural analysis indicated a small fracture between the samples of different ratios which can be attributed to the method used to prepare as well as the shifting of the  $Al^{3+}$  ions. The UV-vis spectroscopy showed variation of energy gap with increasing aluminum concentration, and an increased optical absorbance as the  $Al^{3+}$  ions were introduced in the samples.**

**Key words:** Scanning kelvins probe microscopy, UV-vis spectroscopy, work function, and absorbance.

## **INTRODUCTION**

Nanoparticles have found a wide application due to their superior electrical and electronic properties. Ferrite nanoparticles being a class of special oxides have also been applied in a wide range of applications ranging from millimeter wave integrated circuitry, to the power handling techniques, permanent magnets up to the magnetic recording media (Valenzuela, 2005, 2012). Due to the evolving data storage techniques in recent times, there has been reduction in bit's dimension towards the nanoscale (Larson et al., 2004; Sbiaa and

Piramanayagam, 2007; Gu et al., 2016). Utilizing the optical and electrical properties of materials, optical recording has been developed (Gu et al., 2016). For instance, plasmonic has data storage on metal nanostructures which has a sharp resonance at a specified wavelength which depends fully on the size and shape of the nanostructure (Mansuripur, 2011).

Mansuripur (2011) notes that, the electronic data storage has been depending on static and dynamic random access memories (SRAM and DRAM), but of

\*Corresponding author. E-mail: [pkamweru@gmail.com](mailto:pkamweru@gmail.com) or [pkkamweru@chuka.ac.ke](mailto:pkkamweru@chuka.ac.ke).

recent the Flash Memory has emerged as a contender in storage technology. Despite of the introduction of the flash disk there has been an increase in challenges such as low capacity, have slow data rates and they retain data for a short period of time which is due to charge leakage. These have therefore created a field for nano-volume materials to solve these challenges. Among the likely candidates of materials that have been used as core in memory devices and continued to elicit much research interests in this area of applications are the ferrites (Priya et al., 2019; Flores-Martinez et al., 2019). Lot of research is devoted to recognize the possibilities to improve the electrical properties in order to make it suitable for applications in electronic devices and microwave industries. The advocacy of nanomaterials has been supported by the idea that as the size of the magnetic materials approaches nanoscale, there is an increase in surface area and this therefore has led to novel phenomena (Yao et al., 2007). Ferrites nanomaterials have also exhibited a high signal-to-noise ratio and thermal stability (Ozawa et al., 2017; Tada et al., 2017), properties that should be ideal to data storage devices.

Al doped cobalt ferrites has been reported as suitable for high frequency applications and magnetic memory devices (Priya et al., 2019) among other applications that requires higher electrical conductivity like in electrodes for supercapacitors (Bhujun et al., 2016). Aluminum doping has shown improved electrochemical performance (Priya et al., 2019). Kumar and Kar (2011) reported Al doped cobalt ferrites as a potential candidate for soft magnet applications such as magnetic recording. Their study observed that aluminum in cobalt ferrites reduces saturation magnetization, coercivity, remanent magnetization and magneto crystalline anisotropy constant, which reveal that the material becomes soft magnetic material with the  $Al^{3+}$  substitution. Waghmare et al. (2017), reported that incorporation of non-magnetic  $Al^{3+}$  ions in cobalt ferrite resulted in decrease of saturation magnetization and coercivity because replacement of  $Fe^{3+}$  by  $Al^{3+}$  ions weakens the sub lattice interaction and lowers the magnetic moment of the unit cell. Furthermore, more studies have shown improvements of properties that are important in data memory by doping Zn ions to cobalt ferrites (Jadhav et al., 2010; Somaiah et al., 2012; Jamil et al., 2017; Nayeem et al., 2017). Most of these studies have focused on optimization of the magnetic properties (Pankhurst et al., 2003; Yao et al., 2007).

This study sought to investigate the effect of a double substituted ferrite, the aluminum and zinc doped cobalt ferrite. The intent has also been refocused to investigate the effect of such substitution to electronic properties specifically the work function, energy band gap and optical properties. The study used sol-gel synthesis method, which enables use of low temperatures and less time consuming besides being one of the methods that

has been widely used in production of materials at nanoscale level (Kahn and Zhang, 2001; Krishna et al., 2012), and the ease of varying the stoichiometry of the samples.

## METHODOLOGY

### Synthesis

Sol-gel method was used to synthesize  $Zn_{1-x}CoFe_{2-x}Al_xO_4$  ( $x = 0.0, 0.2, 0.4, 0.6, 0.8$  &  $1.0$ ). All the chemicals were of analytical reagent grade (AR) with 99% purity and supplied by Sigma Aldrich Laboratory Supplies. The varied stoichiometry of the Ferric Nitrate nanohydrate ( $Fe(NO_3)_3 \cdot 9H_2O$ ), Cobalt nitrate hexahydrate ( $Co(NO_3)_2 \cdot 6H_2O$ ), Aluminum nitrate nonahydrate- $Al(NO_3)_3 \cdot 9H_2O$  and Zinc nitrate hexahydrate- $Zn(NO_3)_2 \cdot 6H_2O$  were calculated into their masses as shown in Table 1.

The weighed amount of metal nitrates were dissolved in 10 ml of pure water and stirred vigorously using a magnetic stirrer to form a salt solution. 2 M Citric acid solution was then added to the salt solution in the ratio 1:1. after heating for 10 min. A red-brownish gel was formed after vigorous stirring for 3 h at  $90^\circ C$ . Further heating continued at  $95^\circ C$  until the gel underwent self autocombustion, leading to formation of a loose massive powder. The product was grinded to fine powder using an agate motor and pestle and calcined at  $650^\circ C$  for 4 h to remove any organic impurity.

### Characterization

The XRD analysis of the synthesized nanoparticles was done by a powder XRD (Bruker D2 Phaser Diffractometer) using a  $CuK\alpha$  radiation at  $\lambda = 1.54060 \text{ \AA}$  operating at a voltage of 30 kV and a current of 10 mA and at a  $2\theta$  range for  $10-90^\circ$  with a sweeping rate of  $2^\circ/\text{min}$ . Scanning Kelvin Probe Microscopy (SKPM) was used to study the work function of the samples. The tip voltage was set between 2.9515 - 3.000 V and the peak-to-peak voltage  $V_{p\text{tip}}$  was 1325.7 mV which was kept constant with mean peak-to-peak voltage  $V_{p\text{tip}}$  of 1422.6 mV. Scanning took place for 200 points in steps of 1 where the backing potential  $V_{b+}$  was in the range  $\pm 5000$ . UV-Visible 1800 from Shimadzu was used to obtain the absorbance of the samples. Part of the sintered powder of the samples of  $Al_xZn_{1-x}CoFe_2O_4$  ferrites were dissolved in pyridine and ethylene glycol in the ratio 1:10 under magnetic stirrer and stirred for 10 minutes for further UV-vis characterization.

## RESULTS

### XRD analysis

The phase and purity of the synthesized  $Zn_{1-x}CoFe_{2-x}Al_xO_4$  samples were examined by the XRD. The observed XRD patterns are shown in Figure 1.

Then normalized diffraction peaks at  $2\theta$  values 30.405, 35.69, 43.473, 53.620, 57.4281 and 62.766 are indexed to (220), (311), (400), (422), (511) and (440) reflection planes of aluminum doped zinc cobalt ferrite respectively. The patterns match well with the JCPDS card No. 22-1086 and confirms a spinel of cubic structure which further shows pure samples were synthesized as no additional peak was recorded. The sharp peaks indicate

**Table 1.** Masses of each nitrate.

Required stoichiometry for $\text{Al}_x\text{Zn}_{1-x}\text{CoFe}_2\text{O}_4$	Mass (g)			
	Ferric nitrate	Cobalt nitrate	Aluminium nitrate	Zinc nitrate
x=0.0	3.0000	2.1611	0.0000	2.2090
x=0.2	3.0000	2.1611	0.5571	1.7672
x=0.4	3.0000	2.1611	1.1142	1.3241
x=0.6	3.0000	2.1611	1.6714	0.8836
x=0.8	3.0000	2.1611	2.2285	0.4418
x=1.0	3.0000	2.1611	2.7856	0.0000

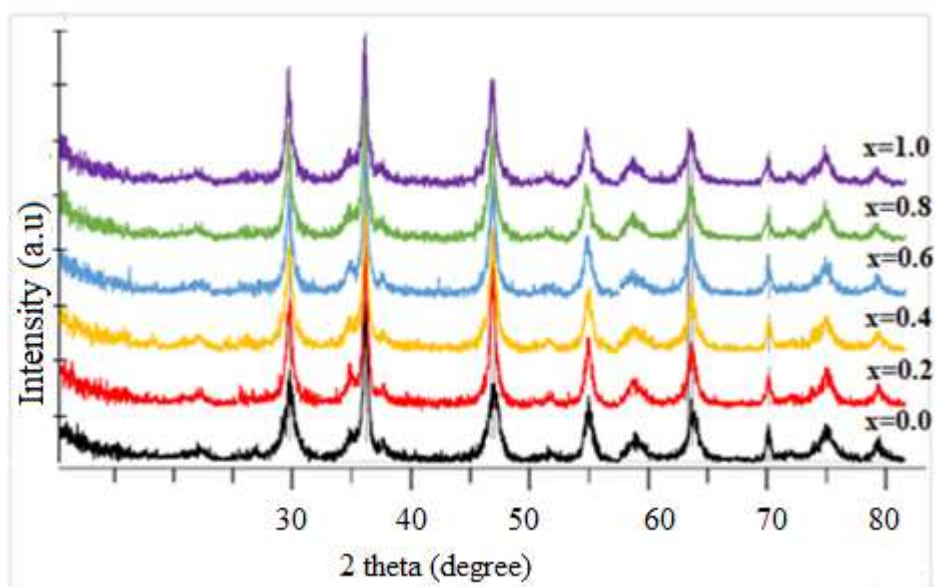


**Figure 1.** XRD patterns of  $\text{Al}_x\text{Zn}_{1-x}\text{CoFe}_2\text{O}_4$  for  $(0 \leq x \leq 1.0)$  for  $x = 0.0$ ,  $x = 0.2$ ,  $x = 0.4$ ,  $x = 0.6$ ,  $x = 0.8$  and  $x = 1.0$ , calcined at  $650^\circ\text{C}$  with most intense peak at  $35.67^\circ$  assigned to 311 from which the equation for crystalline size has been calculated.

a high degree of crystallization. The doping cations therefore, were well incorporated in the precursors. For the spinel cubic structure, the lattice parameter,  $a$ , was determined from the intense peak (311) reflection on the XRD pattern by the use of the equation,  $a = \frac{d_{hkl}}{\sqrt{\frac{h^2+k^2+l^2}{3}}}$ .

The crystalline size  $D$  was determined from the formula,  $D = \frac{0.9\lambda}{\beta \cos \theta}$ .

Evidently the particle size and the lattice parameter decreases with increase of Aluminum concentration. This may be due to the substitution of  $\text{Al}^{3+}$  ions that are smaller than the  $\text{Fe}^{3+}$  ions (Table 2). It could also be as a result of cation redistribution and migration of some  $\text{Al}^{3+}$  ions from the tetrahedral to octahedral sites, orchestrating some  $\text{Zn}^{2+}$  and  $\text{Co}^{2+}$  to migrate from octahedral to tetrahedral sites. This would further cause a smaller bond between the cations, and hence reduced lattice constant and smaller cubic spinel structure. Similar

behavior has been also reported for  $\text{CoAl}_{0.2}\text{Fe}_{1.8}\text{O}_4$  (Chae et al., 2004; Ansari et al., 2016).

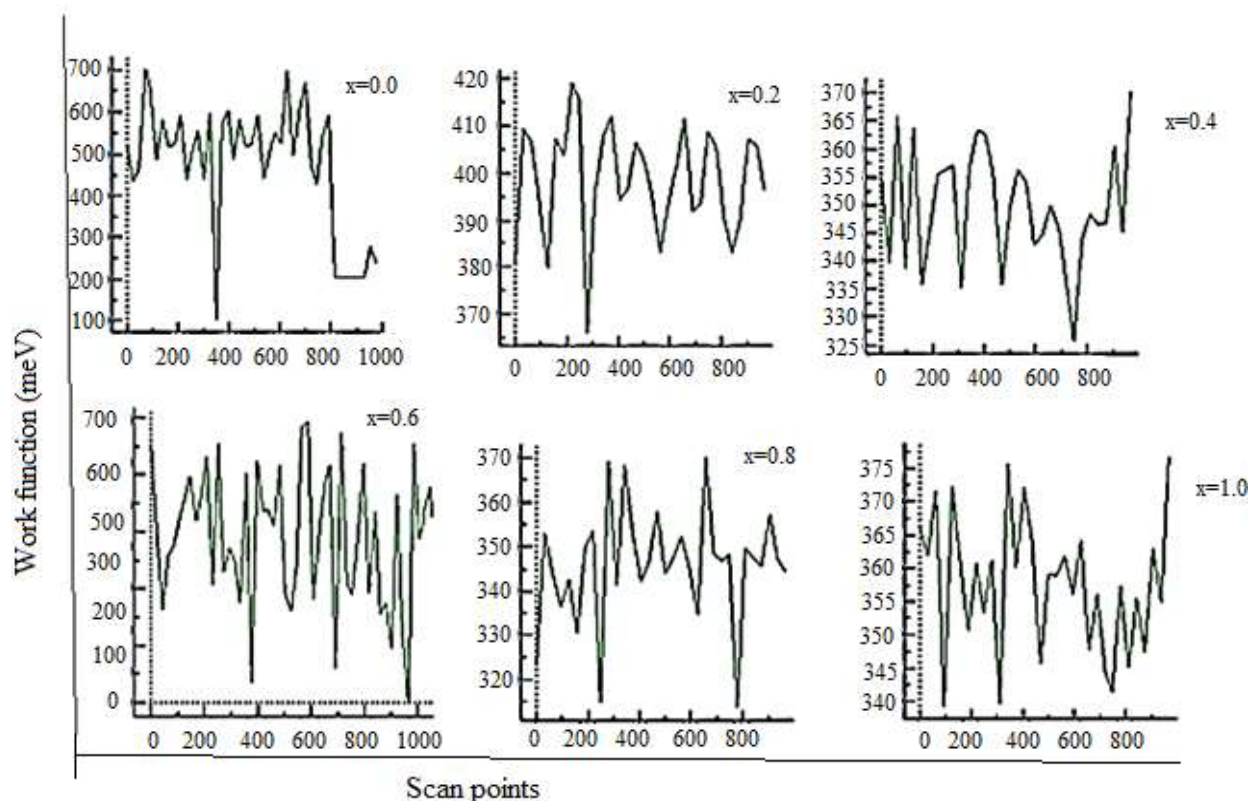
### SKPM Line and area scans

The SKPM images of the line and area scans in Figure 2 and 3 respectively shows that a low work function, in the range of 300-680 meV, which changes with concentration of the dopant Aluminum. This could be attributed to the change of electron distribution on the surface of the samples. There is an increase in the number of electrons as the concentration of the dopant increases. Much of the values are having averagely a lower work function which is an important factor in application in electronics.

Figure 3 shows that doping has an effect on work function; this is depicted by the variation of the surface profiles at different concentrations. The surface formation or reconstruction could be an issue to account for

**Table 2.** The approximate particle size for the different concentration.

Concentration of Aluminum	d- Spacing	Lattice constant(Å)	Approximate size (Nm)
x =0.0	0.6379075	2.1157	76.7442
x =0.2	0.6378472	2.1155	63.4800
x =0.4	0.6377568	2.1152	51.8533
x =0.6	0.6377266	2.1151	44.4444
x=0.8	0.6377266	2.1151	38.8889
x =1.0	0.6376362	2.1148	22.2222

**Figure 2.** Average line from the area scans which reveals that the work function of the samples (for the different values of x) in the samples is between 300-680 meV. This makes the material applicable as semiconductors (Horcas et al., 2007).

variation of the work function. This variation may be caused by a number of factors such as the surface morphology, chemical composition of the sample and the structure of the material. For instance, a shift in surface molecular orientation of a sample or a small amount of contaminant on the surface can bring a significant shift in the work function and impact the electronic structure of interfaces. Much of the values are having an averagely lower work function as shown in Figure 4, which is an important factor in application in electronics. From Figure 4, the work function varied as concentration changes which can be as a result of doping. The line scans work

function is higher due to the distribution of the electrons on the surface of the material. This is because the line scan is in one dimension while the area scan is in 2 dimension and therefore the area scan covers a large surface of scan giving more accurate work function values. This is therefore a prediction of the further lower work function of the samples indicating a good application in transmission storage devices.

The work function against the concentration for the line and area scans were plotted and represented as in the Figure 4. The work function seems to takes a drop when the concentration of  $Zn^{2+}$  and  $Al^{3+}$  cations are around

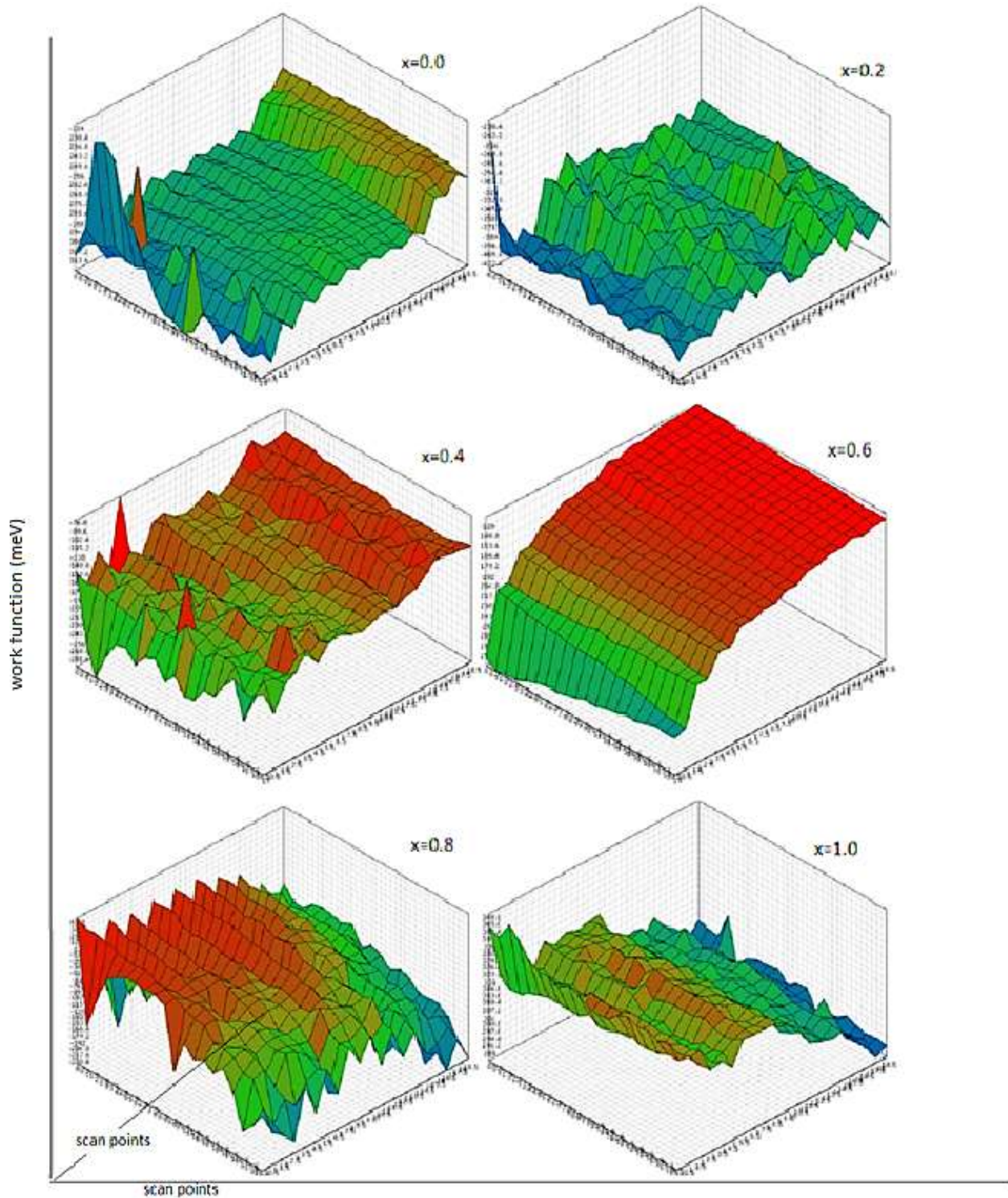


**Figure 3.** Area scan work functions of the samples for different values of  $x$  (Horcas et al., 2007). As the value of  $x$  increases there is a change of the work function averagely up to a certain point for  $x=0.4$  and  $x=0.6$  where the work function starts reducing up to the original value. This creates a trend observable due to increase in the number of electrons up to the optimum value.

50:50. This could be as a result of the changing ratios of the cations species. Zinc has a slightly higher work

function (4.31) than Aluminum (4.28) (Stössel et al., 1999).

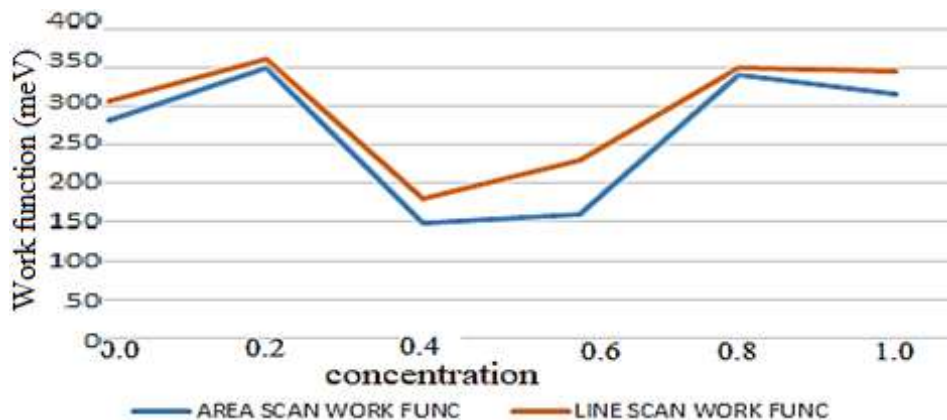


**Figure 4.** Work function against aluminum concentration for both line and area scans for different samples.

### SKPM hole density and fractural analysis

The hole density fractural analysis and the multicellular observation were calculated and viewed in WSxM 4.0 Beta 9.1 by Horcas et al. (2007) and are shown in Figures 5 and 6. The holes were averagely a distance of 251.969 nm from each closest neighbor with an average hole area of 976.562 nm<sup>2</sup> and hole volume of 489.16 nm<sup>3</sup>. The hole density is observed to be uniform throughout the samples which implies that doping does not influence the hole distribution.

The size of holes also increases with increase in aluminum content. The multicellular view reveals that the cell view changes as the value of  $x$  also varies from 0.0 to 1.0. The multicellular view and the hole density were observed by the WSxM 4.0 Beta 9.1 (Horcas et al., 2007). It can also be observed that there is no big different in the fracture of the samples as the aluminum content increase. The average diversion from the neutral axis is equidistant.

The fractural analysis shown in Figure 6 indicates there is less fractures formed as the content of Al<sup>3+</sup> increases. This is can be observed from a small variation of the fracture graph from the average graph. Which can be attributed to the smaller ionic radius of 0.675 Å of Aluminum as compared to 0.88 Å of zinc, this therefore indicates that Aluminum ions can substitute zinc, fitting well in the octahedral and tetrahedral sites (Shannon, 1976).

This is can be observed from a small variation of the fracture graph from the average graph. The size of holes also increases with increase in aluminum content; this is due to the larger ionic radius of Al<sup>3+</sup> as compared to zinc. This therefore suggests a good material to be used in semiconductor devices such as storage devices and information transmission devices. This is further supported by the behavior of cobalt being a semiconductor at some temperatures and a conductor at

some temperatures.

### Energy band gap calculations from SKPM

From the Energy Band Diagrams in the Figures 7, it was realized that as zinc ion are introduced in the sample, the fermi level  $E_f$  was observed rising towards the conduction band  $E_c$ . It is further observed that the fermi level rises into the conduction band predicting the super conductivity of the materials.

In general, the fermi level  $E_f$  found at the middle point of the conduction band  $E_c$  and the valence band  $E_v$  when impurities are introduced in the sample, the fermi level shift either towards or away from the conduction band depending on the conductivity nature of the dopant (Akhtar et al., 2015).

### UV-visible analysis

Figure 8 shows the UV-vis absorption spectrum (in the range of 280 nm-800 nm) of the sol-gel synthesized nanocrystals of Aluminum doped zinc cobalt ferrites which is a function of wavelength in nanometers (nm).

The spectrum for different samples is characterized by 1 to 2 major peaks which are in the range of 304-340 nm. There is observed shift of the wavelength from 340-304; this is attributed to the decrease in particle size (Gharibshahi et al., 2017). There are strong absorption peaks seen as the content of Aluminum is increasing from 304 nm among the samples with a high absorbance is at 340 nm which has the highest content for the Al<sup>3+</sup> ions absorbance (Akhtar et al., 2015). The maximum absorbance is well explained by Mie theory both classically and traditionally. In metal nanoparticle, electrons in the conduction band or near the surface are excited an effect called surface Plasmon response (Desai

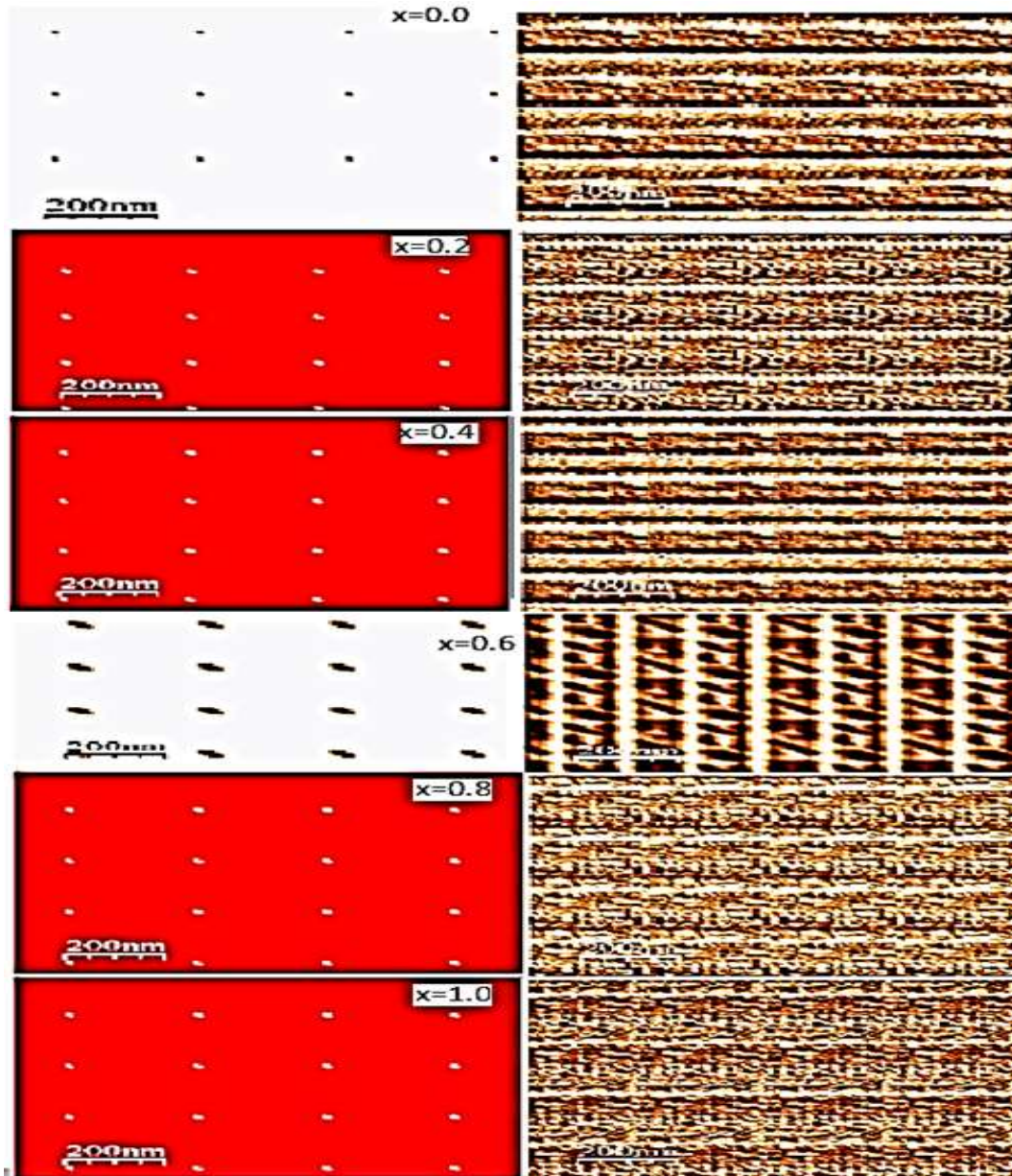


**Figure 4.** The hole density and the multicellular simulations plots at a magnification of 200 nm (Horcas et al., 2007). The hole density was found to be 16 holes per multiple cell analysis.

et al., 2012); the optical absorption of metal nanoparticles can be described quantum mechanically due to intra-band interactions emulating the interaction of light energy on metal surface through Compton scattering and photoelectric effect (Gharibshahi et al., 2017). Aluminium has a higher plasma frequency which finds application in surface plasma responses. It can be observed that as the aluminum content was being increased there was a reduction in absorbance as depicted by spectra of  $x=0.0$  and  $x=1.0$ . This can be attributed to the cation distribution in the sample.

Absorbance against the energy absorbed was found to

be as in Figure 9. From the spectrum the energy absorbed is inversely proportional to the wavelength.

The samples were observed to be between 1.85 to 4.2 eV; this is because the spectrum starts to rise from these region (Holinsworth et al., 2013). The samples start absorbing energy from 1.85 eV; this is due to the indirect band gap of O-Fe-O present in the sample (Holinsworth et al., 2013). At the 2.86 eV value, there is a direct band gap which is associated with the  $\text{CoFe}_2\text{O}_4$  present in the sample. As seen from the spectrum in Figure 9, there is a strong energy gap as absorbance increases; this is attributed to the continued combination of the Aluminium

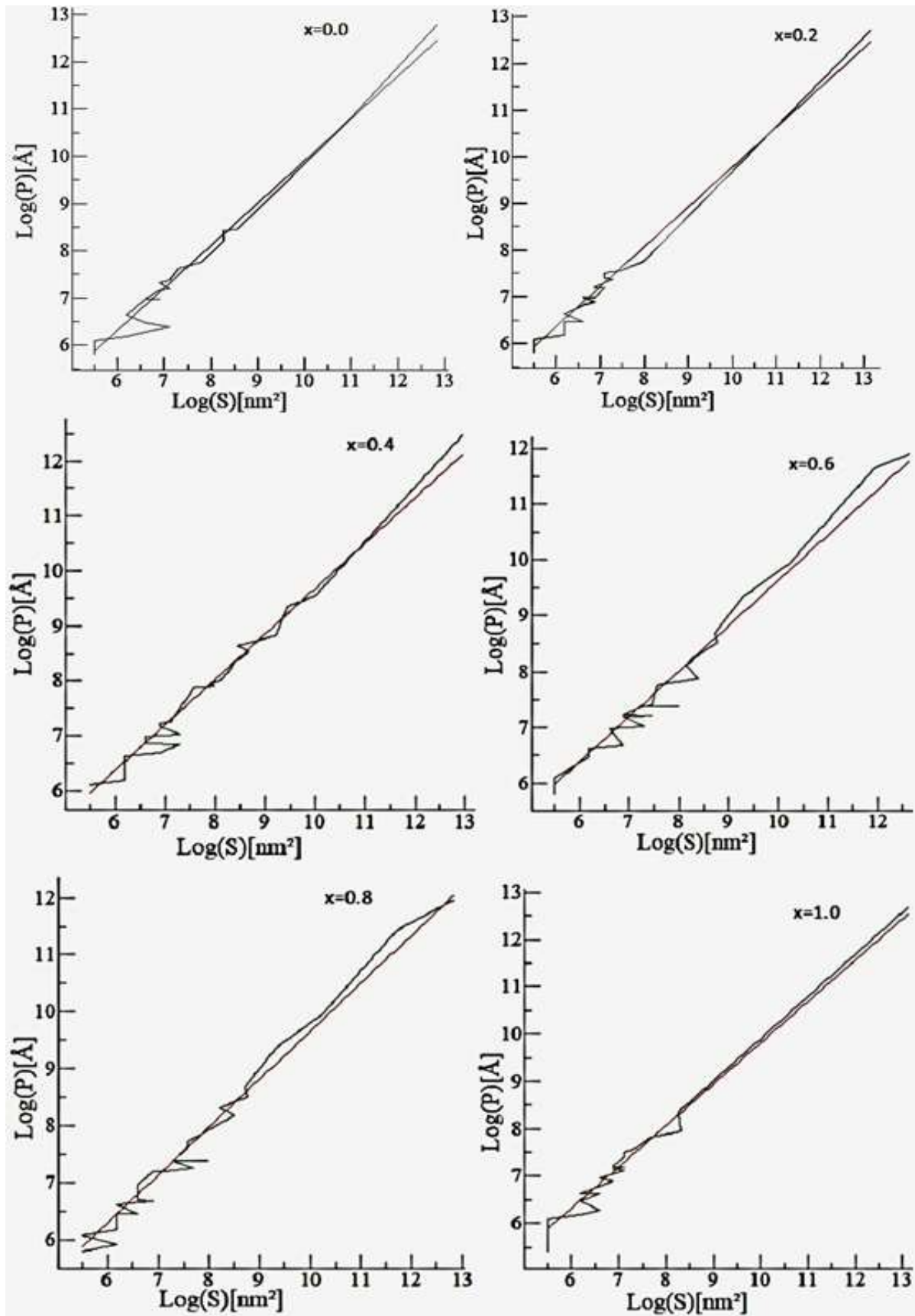
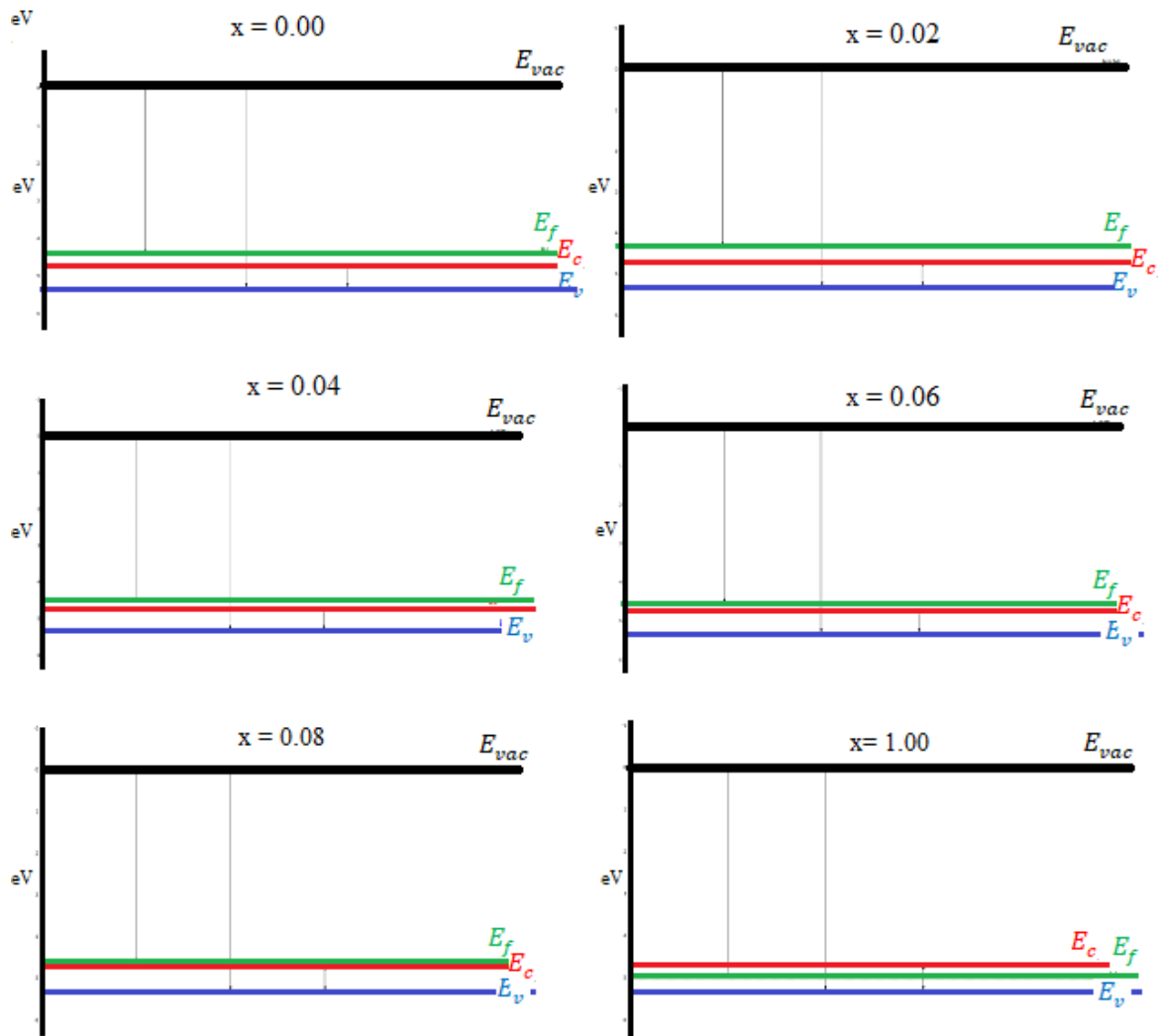
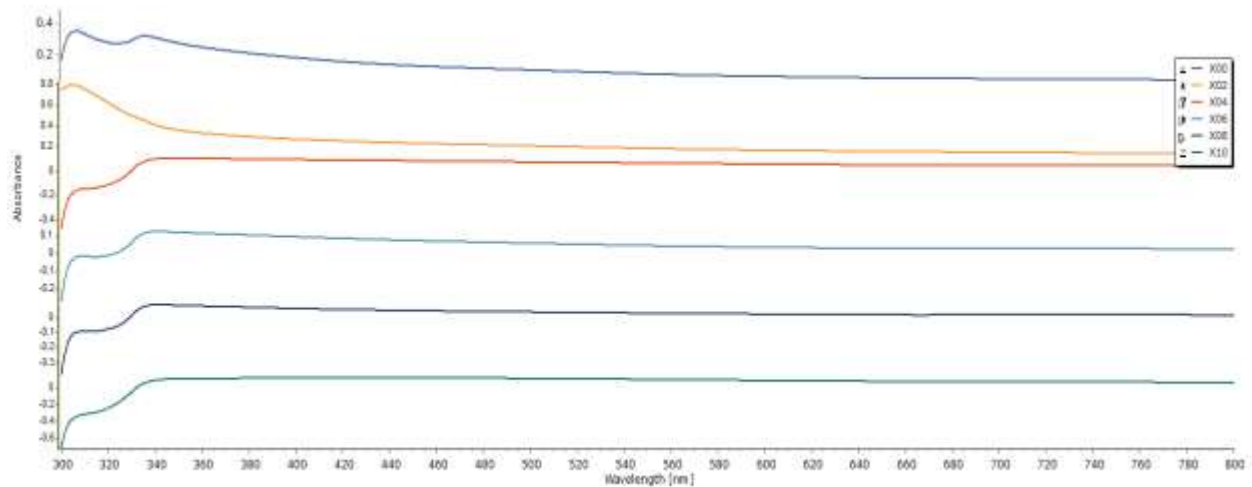


Figure 6. The fractal analysis.



**Figure 7.** The energy level diagrams for the samples  $\text{Zn}_{1-x}\text{CoFe}_{2-x}\text{Al}_x\text{O}_4$  ( $x=0.00, 0.02, 0.04, 0.06, 0.08$  and  $1.00$ ).



**Figure 8.** UV visible spectrum for the samples of  $\text{Zn}_{1-x}\text{CoFe}_{2-x}\text{Al}_x\text{O}_4$  ( $x = 0.0, 0.2, 0.4, 0.6, 0.8$  and  $1.0$ ).

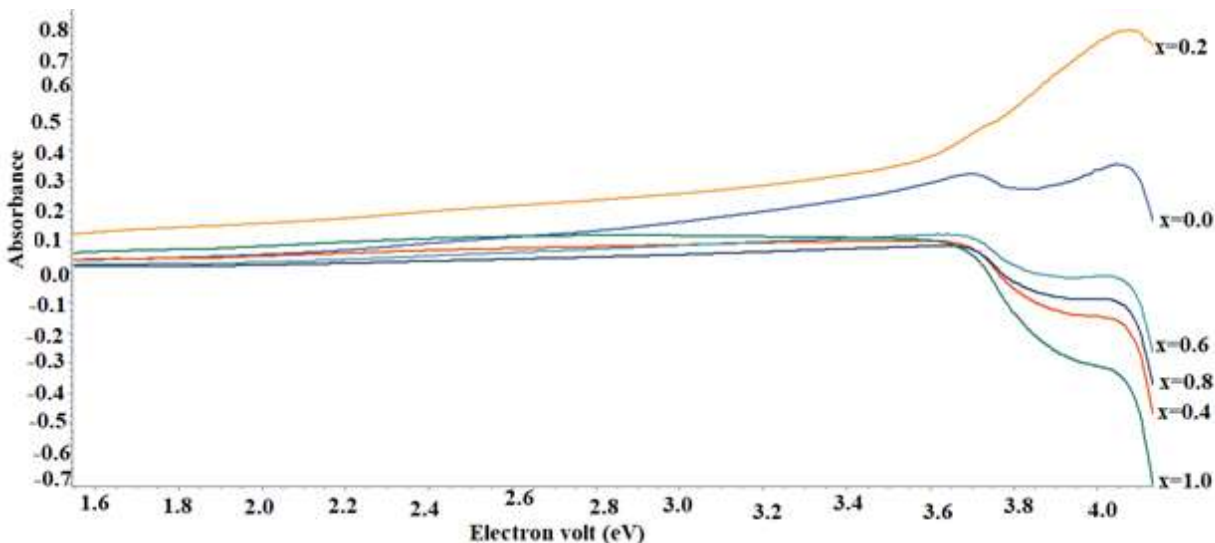


**Figure 9.** Absorbance versus electron volt showing the energy absorbed by the samples when they are subjected to the ultraviolet radiations.

ions with the cobalt and ferric ions (Holinsworth et al., 2013). The excitation within 3 eV are attributed to the O 2p to Fe 3p charge transfer excitations (Rai et al., 2012); the  $\text{Co}^{2+} (3d)^7$  shifts to the octahedral sites while the  $\text{Fe}^{3+}(3d)^5$  t are shifts to occupy the tetrahedral site and octahedral sites equally (Rai et al., 2012). Generally, there is high absorbance which decreases as the  $\text{Al}^{3+}$  ions increases. This is attributed to the crystal structure of ferrites formed. The sample  $x=0.2$  has the highest absorbance followed by the sample  $x=0.0$ . The sample with  $x=1.0$  had the lowest absorbance which is due to the absence of the zinc ions in the sample. There was negative absorbance which could be attributed to the noise in the measuring instrument or light source exciting the samples to excite larger energy emissions which could cause emergent emissions exceeding the incident light and can also be due to differences in refractive index (Ji et al., 2016). This gives the samples  $x=0.0$ , 0.2 and 0.6 candidature for the application in storage devices. This predicts their ability for the device to absorb information either in magnetic or optical nature.

## CONCLUSION AND RECOMMENDATION

The electronic and optical properties of Aluminum doped zinc cobalt ferrite nanoparticles were studied using the Scanning Kelvin Probe Microscopy and the UV-vis spectroscopy. The work function from the area and line scans from the kelvins probe was found to be reduced from 680 to 300 meV with sample of  $x=0.6$  recording the lowest work function. Likewise, the absorption from the UV-vis was also found to be in the range of 304-340 nm in wavelength range. The energy absorbed when the

ultra violet radiations are directed to the sample was found to range from 1.85-4.08 which was attributed to re alignment of the aluminum, ferric and cobalt ions as well as zinc and oxygen ions in the sample to A and B sites. The addition of aluminum did not cause a significant fracture in the alignment of the ferrite particles; the increase in the size of the hole as the aluminum content increases can be attributed to the larger ionic radius of the aluminum ions. The hole density was maintained making the ferrite a better candidate for application in the storage, recording, transmission and memory devices. It is therefore clear aluminum doping in ferric nanoparticles bring about change in the energy absorbed, band gap and the work function as well as making the ferrite applicable in a wide range of electronic devices.

## CONFLICT OF INTERESTS

The authors have not declared any conflict of interests.

## REFERENCES

- Akhtar MJ, Alhadlaq HA, Alshamsan A, Khan MM, Ahamed M (2015). Aluminum doping tunes band gap energy level as well as oxidative stress-mediated cytotoxicity of ZnO nanoparticles in MCF-7 cells. *Scientific Reports* 5(1):1-16. <https://doi.org/10.1038/srep13876>
- Ansari S, Arabi H, Sadr SMA (2016). Structural, Morphological, Optical and Magnetic Properties of Al-Doped  $\text{CoFe}_2\text{O}_4$  Nanoparticles Prepared by Sol-Gel Auto-Combustion Method. *Journal of Superconductivity and Novel Magnetism* 29(6):1525-1532. <https://doi.org/10.1007/s10948-016-3423-4>
- Bhujun B, Tan MT, Shanmugam AS (2016). Evaluation of aluminium doped spinel ferrite electrodes for supercapacitors. *Ceramics International* 42(5):6457-6466. <https://doi.org/10.1016/j.ceramint.2015.12.118>
- Chae KP, Lee JG, Kweon HS, Lee YB (2004). The crystallographic,

- magnetic properties of Al, Ti doped  $\text{CoFe}_2\text{O}_4$  powders grown by sol-gel method. *Journal of Magnetism and Magnetic Materials*, 283(1):103-108. <https://doi.org/10.1016/j.jmmm.2004.05.010>
- Desai R, Mankad V, Gupta SK, Jha PK (2012). Size distribution of silver nanoparticles: UV-visible spectroscopic assessment. *Nanoscience and Nanotechnology Letters* 4(1):30-34. <https://doi.org/10.1166/nnl.2012.1278>
- Flores-Martinez N, Franceschin G, Gaudisson T, Haj-Khlifa S, Derouich SG, Yaacoub, N, Ammar S. (2019). On the first evidence of exchange-bias feature in magnetically contrasted consolidates made from  $\text{CoFe}_2\text{O}_4$ -CoO core-shell nanoparticles. *Scientific Reports*, 9. <https://doi.org/10.1038/s41598-019-55649-y>
- Gharibshahi L, Saion E, Gharibshahi E, Shaari AH, Matori KA (2017). Structural and optical properties of Ag nanoparticles synthesized by thermal treatment method. *Materials* 10(4):402.
- Gu M, Zhang Q, Lamon S. (2016). Nanomaterials for optical data storage. *Nature Reviews Materials* 1(12):1-14. <https://doi.org/10.1038/natrevmats.2016.70>
- Holinsworth BS, Mazumdar D, Sims H, Sun QC, Yurtisigi, MK, Sarker SK, Musfeldt JL. (2013). Chemical tuning of the optical band gap in spinel ferrites:  $\text{CoFe}_2\text{O}_4$  vs  $\text{NiFe}_2\text{O}_4$ . *Applied Physics Letters* 103(8):082406. <https://doi.org/10.1063/1.4818315>
- Horcas I, Fernández R, Gomez-Rodríguez JM, Colchero JWSX, Gómez-Herrero JWSXM, Baro AM (2007). WSXM: A software for scanning probe microscopy and a tool for nanotechnology. *Review of Scientific Instruments* 78(1):013705 <https://doi.org/10.1063/1.2432410>
- Jadhav SS, Shirsath SE, Patange SM, Jadhav KM (2010). Effect of Zn substitution on magnetic properties of nanocrystalline cobalt ferrite. *Journal of Applied Physics* 108(9):093920. <https://doi.org/10.1063/1.3499346>
- Jamil MT, Ahmad J, Bukhari SH., Sultan T, Akhter MY, Ahmad H, Murtaza G. (2017). Effect on structural and optical properties of Zn-substituted cobalt ferrite  $\text{CoFe}_2\text{O}_4$ . *Journal of Ovonic Research* 13(1):45-53.
- Ji Y, Ji Z, Yao M, Qian Y, Peng Y (2016). Negative absorption peaks in ultraviolet-visible spectrum of water. *Chemistry Select* 1(13):3443-3448. <https://doi.org/10.1002/slct.201600587>
- Kahn ML, Zhang ZJ (2001). Synthesis and Magnetic Properties of  $\text{CoFe}_2\text{O}_4$  Spinel Ferrite Nanoparticles Doped with Lanthanide Ions. *Applied Physics Letters* 78(23):3651-3653. <https://doi.org/10.1063/1.1377621>
- Krishna KR, Ravinder D, Kumar KV, Lincon CA (2012) Synthesis, XRD and SEM Studies of Zinc Substitution in Nickel Ferrites by Citrate Gel Technique. *World Journal of Condensed Matter Physics* 2:153-159. <http://dx.doi.org/10.4236/wjcmp.2012.23025>.
- Kumar L, Kar M (2011). Influence of  $\text{Al}^{3+}$  ion concentration on the crystal structure and magnetic anisotropy of nanocrystalline spinel cobalt ferrite. *Journal of Magnetism and Magnetic Materials* 323(15):2042-2048. <https://doi.org/10.1016/j.jmmm.2011.03.010>
- Larson DJ, Petford-Long AK, Ma YQ, Cerezo A (2004). Information storage materials: Nanoscale characterisation by three-dimensional atom probe analysis. *Acta Materialia* 52(10):2847-2862. <https://doi.org/10.1016/j.actamat.2004.03.015>
- Mansuripur M (2011, July). The role of nano-technology in data storage devices and systems. In *Joint International Symposium on Optical Memory and Optical Data Storage* (p. OMA2). Optical Society of America.
- Nayeem F, Parveez A, Chaudhuri A, Sinha RR, Khader SA (2017). Effect of  $\text{Zn}^{2+}$  doping on structural, dielectric and electrical properties of cobalt ferrite prepared by auto combustion method. *Materials Today: Proceedings* 4(11):12138-12143. <https://doi.org/10.1016/j.matpr.2017.09.142>
- Ozawa E, Musha A, Morooka A, Oyanagi M, Tada T, Suzuki H (2017). Development of Barium Ferrite Tape with a High Signal-to-Noise Ratio and Thermal Stability. *IEEE Transactions on Magnetics* 54(2):1-4. DOI:10.1109/TMAG.2017.2746138
- Pankhurst QA, Connolly J, Jones SK, Dobson JJ (2003). Applications of magnetic nanoparticles in biomedicine. *Journal of Physics D: Applied Physics* 36(13):R167. <https://doi.org/10.1088/0022-3727/36/13/201>
- Priya AS, Geetha D, Kavitha N (2019). Effect of Al substitution on the structural, electric and impedance behavior of cobalt ferrite. *Vacuum* 160:453-460. <https://doi.org/10.1016/j.vacuum.2018.12.004>
- Rai RC, Wilser S, Guminiak M, Cai B, Nakarmi ML (2012). Optical and electronic properties of  $\text{NiFe}_2\text{O}_4$  and  $\text{CoFe}_2\text{O}_4$  thin films. *Applied Physics A* 106(1):207-211. <https://doi.org/10.1007/s00339-011-6549-z>
- Sbiaa R, Piramanayagam SN (2007). Patterned media towards nano-bit magnetic recording: Fabrication and challenges. *Recent Patents on Nanotechnology* 1(1):29-40. <https://doi.org/10.2174/187221007779814754>
- Shannon RD (1976). Revised effective ionic radii and systematic studies of interatomic distances in halides and chalcogenides. *Acta crystallographica section A: Crystal Physics, Diffraction, Theoretical and General Crystallography* 32(5):751-767. <https://doi.org/10.1107/S0567739476001551>
- Somaiah N, Jayaraman TV, Joy PA, Das D (2012). Magnetic and magnetoelastic properties of Zn-doped cobalt-ferrites— $\text{CoFe}_{2-x}\text{Zn}_x\text{O}_4$  (x= 0, 0.1, 0.2, and 0.3). *Journal of Magnetism and Magnetic Materials* 324(14):2286-2291. <https://doi.org/10.1016/j.jmmm.2012.02.116>
- Stössel M, Staudigel J, Steuber F, Simmerer J, Winnacker A (1999). Impact of the cathode metal work function on the performance of vacuum-deposited organic light emitting-devices. *Applied Physics A* 68(4):387-390. DOI 10.1007/s003399900011
- Tada T, Suzuki H, Shimizu O (2017). *U.S. Patent No. 9,818,517*. Washington, DC: U.S. Patent and Trademark Office. Valenzuela, R. (2005). *Magnetic Ceramics* (Vol. 4). Cambridge University Press.
- Valenzuela R (2012). Novel applications of ferrites. *Physics Research International*, 2012. doi:10.1155/2012/591839
- Yao C, Zeng Q, Goya GF, Torres T, Liu J, Wu H, Jiang JZ (2007).  $\text{ZnFe}_2\text{O}_4$  nanocrystals: synthesis and magnetic properties. *The Journal of Physical Chemistry C* 111(33):12274-12278. <https://doi.org/10.1021/jp0732763>.